

The temperature-dependent conformational ensemble of SARS-CoV-2 main protease (M^{pro})Ali Ebrahim,^{a,b,‡} Blake T. Riley,^{b,‡} Desigan Kumaran,^c Babak Andi,^{d,e} Martin R. Fuchs,^d Sean McSweeney^{d,e} and Daniel A. Keedy^{b,f,g,*}

Received 12 May 2022

Accepted 21 July 2022

Edited by E. N. Baker, University of Auckland, New Zealand

‡ These authors contributed equally to this work.

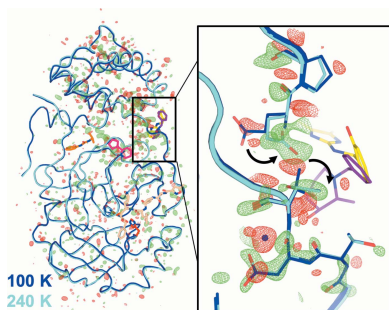
Keywords: protein structure; protein flexibility; X-ray crystallography; allostery; SARS-CoV-2 main protease; temperature-dependent; COVID-19.**PDB references:** SARS-CoV-2 M^{pro} multiconformer model, 7mhf; 7mhg; 7mhh; 7mhi; 7mhj; 7mhk; ensemble model, 7mhl; 7mhm; 7mhn; 7mho; 7mhp; 7mhq**Supporting information:** this article has supporting information at www.iucrj.org^aDiamond Light Source, Harwell Science and Innovation Campus, Didcot, OX11 0DE, England, United Kingdom, ^bStructural Biology Initiative, CUNY Advanced Science Research Center, New York, NY 10031, USA, ^cBiology Department, Brookhaven National Laboratory, Upton, NY 11973, USA, ^dCenter for BioMolecular Structure, NSLS-II, Brookhaven National Laboratory, Upton, NY 11973, USA, ^eNational Virtual Biotechnology Laboratory (NVBL), US Department of Energy, Washington, DC, USA, ^fDepartment of Chemistry and Biochemistry, City College of New York, New York, NY 10031, USA, and ^gPhD Programs in Biochemistry, Biology, and Chemistry, The Graduate Center—City University of New York, New York, NY 10016, USA. *Correspondence e-mail: dkeedy@gc.cuny.edu

The COVID-19 pandemic, instigated by the SARS-CoV-2 coronavirus, continues to plague the globe. The SARS-CoV-2 main protease, or M^{pro}, is a promising target for the development of novel antiviral therapeutics. Previous X-ray crystal structures of M^{pro} were obtained at cryogenic temperature or room temperature only. Here we report a series of high-resolution crystal structures of unliganded M^{pro} across multiple temperatures from cryogenic to physiological, and another at high humidity. We interrogate these data sets with parsimonious multiconformer models, multi-copy ensemble models, and isomorphous difference density maps. Our analysis reveals a perturbation-dependent conformational landscape for M^{pro}, including a mobile zinc ion interleaved between the catalytic dyad, mercurial conformational heterogeneity at various sites including a key substrate-binding loop, and a far-reaching intramolecular network bridging the active site and dimer interface. Our results may inspire new strategies for antiviral drug development to aid preparation for future coronavirus pandemics.

1. Introduction

COVID-19 is a global pandemic disease caused by severe acute respiratory syndrome coronavirus 2. SARS-CoV-2 is a highly infectious airborne respiratory virus which has caused over 580 million infections and over 6.4 million deaths worldwide as of August 2022. Over the past two years, several approaches to prevent and treat COVID-19 have been successfully developed, including new vaccines, monoclonal antibody treatments (Baum *et al.*, 2020), and repurposed existing therapeutics (Beigel *et al.*, 2020; Boras *et al.*, 2021). More recently, small-molecule antiviral drugs have fortunately been approved for clinical use to combat COVID-19. Notwithstanding these successes, additional chemical tools to modulate the function of coronavirus proteins would aid in the preparation for future coronavirus pandemics.

A promising target for potential new antiviral drugs against SARS-CoV-2 is a chymotrypsin-like protease known by several names: non-structural protein 5, nsp5, 3C-like protease, 3CL^{pro}, main protease, or M^{pro}. M^{pro} is part of a polyprotein encoded by the viral RNA genome. After being excized from the polyprotein by its own proteolytic activity, M^{pro} cleaves at no fewer than 11 sites in the polyprotein to generate individual functional proteins (V'kovski *et al.*, 2021) that help the virus replicate. Due to its importance to the



OPEN ACCESS

Published under a CC BY 4.0 licence

SARS-CoV-2 life cycle, M^{Pro} has been identified as a key target for COVID-19 drug design.

Drug design efforts focused on M^{Pro} have been aided by insights from structural biology. The first SARS-CoV-2 M^{Pro} crystal structures were released in the Protein Data Bank (PDB; Berman *et al.*, 2000) early in the pandemic, within the first week of February 2020 (Jin *et al.*, 2020). These structures revealed that, like SARS-CoV M^{Pro} before it, SARS-CoV-2 M^{Pro} is composed of two β -barrel domains known as domain I and domain II, and an α -helical bundle known as domain III [Fig. 1(a)]. The active-site cavity is located on the surface, with the His41-Cys145 catalytic dyad positioned between domain I and domain II. Domain III is involved in regulating dimerization (Zhang *et al.*, 2020), which is critical for coronavirus M^{Pro} catalytic activity (Fan *et al.*, 2004; Goyal & Goyal, 2020). Since the initial structures of SARS-CoV-2 M^{Pro}, X-ray crystallography has been used to identify promising ligand-binding sites and alternate structural states of the protein, resulting in a total of over 310 available structures. These efforts included

cocrystallography with an eye toward drug repurposing (Vuong *et al.*, 2020; Günther *et al.*, 2021), as well as crystallographic screens of noncovalent and covalent small-molecule fragments to establish new footholds for *ab initio* drug design (Douangamath *et al.*, 2020), which were then leveraged *via* a crowdsourced process to design novel inhibitors (Chodera *et al.*, 2020).

As with much modern protein crystallography, the above experiments were performed at cryogenic temperatures, which can bias protein conformational ensembles (Fraser *et al.*, 2011; Keedy *et al.*, 2014). To bypass this limitation, a room-temperature crystal structure of unliganded M^{Pro} was reported (Kneller, Phillips, O'Neill, Jedrzejczak *et al.*, 2020) (PDB entry 6wqf), although its resolution was only moderate (2.3 Å) and the conclusions of the article about the effects of cryogenic *versus* room temperature were later questioned (Jaskolski *et al.* 2021). Subsequent work built on this foundation of room-temperature crystallography to dissect M^{Pro} function (Kneller, Phillips, Kovalevsky *et al.*, 2020; Kneller, Phillips, O'Neill, Tan *et al.*, 2020). However, no studies to date have reported crystal structures of M^{Pro} across a wide range of temperatures. Previously, such a multitemperature crystallography strategy was instrumental for revealing novel aspects of correlated active-site conformational heterogeneity in a dynamic proline isomerase (Keedy *et al.*, 2015) and of long-range allosteric signaling in a therapeutic target tyrosine phosphatase (Keedy *et al.*, 2018).

Here we report high-resolution crystal structures of SARS-CoV-2 M^{Pro} at five temperatures: 100 (cryogenic), 240 (above the so-called glass transition or dynamical transition; Keedy *et al.*, 2015), 277 ('room temperature' in many crystallography studies), 298 (ambient), and 310 K (physiological). We also report a structure at ambient temperature but high relative humidity (99.5% RH) to gauge the relative effects of temperature *versus* humidity on M^{Pro}. To our knowledge, this study represents the first experimentally based structural analysis for any SARS-CoV-2 protein at variable temperature and/or humidity. We used careful data collection with a helical strategy to minimize radiation damage, thereby isolating the effects of temperature and humidity on M^{Pro}. For all data sets we have constructed parsimonious multiconformer models, as well as multi-copy crystallographic ensemble models, which provide complementary insights into protein structural flexibility as a function of temperature and humidity. Together, our data reveal a network of subtle but provocative temperature-dependent conformational heterogeneity spanning several functionally relevant sites throughout M^{Pro}, which may help motivate an allosteric strategy for antiviral drug design to aid the preparation for future coronavirus pandemics.

2. Results

2.1. Multitemperature crystallographic data collection and modeling

Data were obtained from single M^{Pro} crystals using helical data collection, to maximize diffraction intensity while minimizing radiation damage (Fig. S1 in the supporting informa-

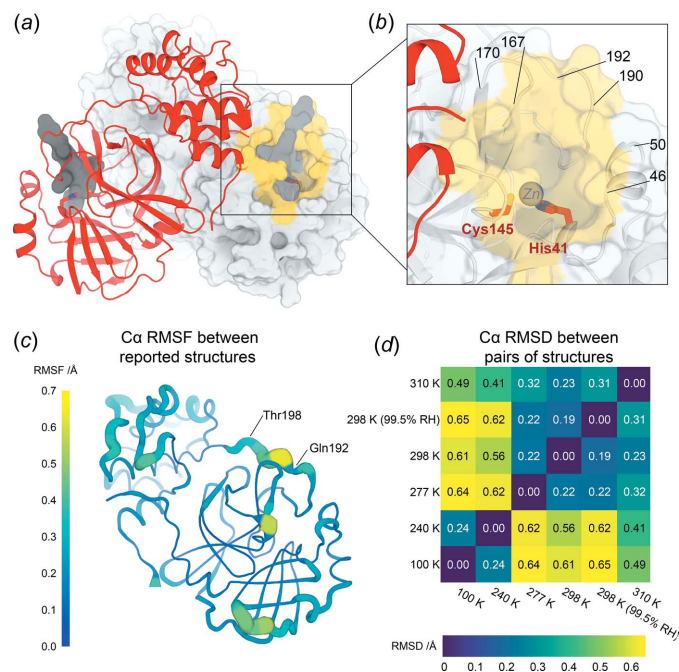


Figure 1

The overall structure of SARS-CoV-2 main protease at multiple temperatures. (a) A new X-ray crystal structure of apo M^{Pro} at physiological temperature (310 K) (red). The biological dimer involving the other monomer (light-gray surface) is constituted *via* crystal symmetry. The competitive inhibitor N3 from a previous structure (PDB entry 6lu7) (semitransparent, dark-gray surface) is shown in both protomers for context. (b) Close-up view of the M^{Pro} active-site region, including the catalytic dyad of Cys145 and His41 (red sticks), and highlighting residues that form the substrate-binding pocket (yellow surface). (c) Cartoon putty representation of conformational variability between new M^{Pro} structures described in this work: 100, 240, 277, 298, 298 (99.5% RH), and 310 K. Thickness and color indicate r.m.s. fluctuations (RMSFs) of the C α -atom positions, from low (thin, dark blue) to high (thick, yellow). The largest differences between the backbones of these structures occur between residues 192–198. Same view as part (a). See also Fig. S3. (d) Heatmap of pairwise C α -atom r.m.s. deviation (RMSD) between the final refined structures, revealing the temperature-dependent clustering (top right *versus* bottom left). See also Fig. S2.

Table 1

Crystallographic statistics for multitemperature data sets and multiconformer models.

Overall statistics given first (statistics for highest-resolution bin in parentheses). RH = relative humidity. RMSD = r.m.s. deviation from ideal values. For *Phenix* ensemble model refinement statistics, see Table 2.

Structure	100 K	240 K	277 K	298 K	298 K, 99.5% RH	310 K
PDB entry	7mhf	7mhg	7mhh	7mhi	7mhj	7mhk
Resolution (Å)	48.07–1.55	55.62–1.53	48.96–2.19	56.29–1.88	56.30–2.00	43.97–1.96
Completeness (%)	99.7 (96.0)	100 (99.4)	99.9 (98.7)	100 (100)	99.0 (97.4)	99.9 (100)
Multiplicity	3.4 (3.4)	6.6 (6.2)	6.9 (6.9)	6.8 (6.9)	6.8 (6.7)	6.6 (6.7)
$I/\sigma(I)$	3.3 (1.0)	7.9 (0.9)	4.5 (1.1)	5.0 (0.4)	6.3 (0.6)	5.4 (0.3)
$R_{\text{merge}}(I)$	0.158 (0.507)	0.180 (1.463)	0.292 (1.805)	0.182 (2.353)	0.178 (1.708)	0.195 (1.805)
$R_{\text{meas}}(I)$	0.188 (0.604)	0.196 (1.600)	0.316 (1.954)	0.197 (2.548)	0.193 (1.854)	0.213 (1.957)
$R_{\text{p.i.m.}}(I)$	0.100 (0.325)	0.076 (0.639)	0.119 (0.742)	0.076 (0.967)	0.074 (0.711)	0.084 (1.046)
$CC_{1/2}$	0.977 (0.695)	0.995 (0.356)	0.985 (0.799)	0.990 (0.285)	0.989 (0.376)	0.990 (0.352)
Wilson B factor	16.164	16.370	31.769	29.670	34.350	33.810
Total observations	127548	263470	97820	152368	125878	128140
Unique observations	37901	39975	14120	22459	18588	19444
Space group	C121	C121	C121	C121	C121	C121
Unit-cell dimensions (Å, °)	113.71, 53.32, 44.57, 90, 102.96, 90	114.19, 53.49, 45.00, 90, 103.04, 90	115.02, 54.36, 44.97, 90, 101.50, 90	114.74, 54.57, 45.11, 90, 101.65, 90	114.88, 54.74, 45.24, 90, 101.42, 90	114.3, 54.29, 44.97, 90, 102.12, 90
Solvent content (%)	35.88	36.40	38.95	39.53	39.89	38.36
R_{work}	0.1821	0.1692	0.1991	0.1906	0.1947	0.1979
R_{free}	0.2242	0.2050	0.2525	0.2276	0.2397	0.2473
RMSD bonds (Å)	0.010	0.014	0.002	0.007	0.002	0.012
RMSD angles (°)	0.962	1.234	0.464	0.649	0.502	0.840
Ramachandran outliers (%)	0.00	0.33	0.33	0.33	0.33	0.66
Ramachandran favored (%)	97.70	98.36	96.38	96.71	96.38	97.04
Clashscore	2.80	1.61	1.68	1.68	0.84	1.68
<i>MolProbity</i> score	1.13	0.91	1.16	1.13	1.00	1.09

tion). To probe the conformational landscape of M^{pro} , we obtained high-resolution structures at five different temperatures: 100, 240, 277, 298 (ambient; see *Methods* section), and 310 K. Our data sets thus span a broad temperature range: cryogenic, just above the glass transition or dynamic transition (Keedy *et al.*, 2015), the range often noted as room temperature (roughly 293–300 K), and approximately physiological temperature. We also collected another 298 K data set with high relative humidity (99.5% RH).

For all but the 277 K data set (2.19 Å), the resolution was 2 Å or better [based on an outer shell $CC_{1/2}$ cut-off of $>\sim 0.3$ (Karplus & Diederichs, 2012); see *Methods* section and Table 1]. The highest resolution was for the 240 K data set (1.53 Å). Even at the higher temperatures, we saw little to no evidence of radiation damage (Fig. S1). After data reduction, we created a multiconformer model for each temperature, which includes a single conformer for most portions of the structure, but alternate conformations where appropriate (Riley *et al.*, 2021). See *Methods* section for more details on data collection and modeling, and Table 1 for the overall diffraction data and refinement statistics.

2.2. Overall structure as a function of temperature

The global structure of M^{pro} in our crystals remains similar across the temperatures [Figs. 1(*d*) and S2], as expected. Indeed, the maximum $C\alpha$ r.m.s. deviation (RMSD) between any pair of structures in the ambient-humidity multitemperature series is only 0.64 Å, and the maximum all-atom RMSD is only 0.95 Å. However, there is a clear clustering between lower-temperature (100 and 240 K) and higher-temperature

(277, 298, and 310 K) structures, based on either $C\alpha$ RMSD [Fig. 1(*d*)] or all-atom RMSD (Fig. S2). These observations indicate that aspects of the M^{pro} conformational landscape change in response to temperature.

Humidity also appears to have some effect on M^{pro} structure, as shown by the fact that the overall largest pairwise $C\alpha$ RMSD [0.65 Å, Fig. 1(*d*)] and all-atom RMSD (1.02 Å, Fig. S2) involve the 298 K high-humidity (99.5% RH) structure. However, the corresponding RMSD values for the 298 K ambient-humidity (36.7% RH) structure are only slightly smaller (<0.1 Å difference). These RMSD differences between high *versus* low humidity are minor compared to the differences between the high- *versus* low-temperature clusters mentioned above. Thus, temperature affects the M^{pro} structure noticeably more than does humidity. This result contrasts with previous studies of lysozyme in which similar structural alterations of the protein were achieved by either small changes in humidity or large changes in temperature (Atakisi *et al.*, 2018); this discrepancy may result from different protein–solvent arrangements in the lysozyme *versus* M^{pro} crystal lattices.

2.3. Temperature dependence of local alternate conformations

To provide more detailed insights into the observed global temperature dependence, we sought to identify alternate conformations at the local scale that were stabilized or modulated by the temperature shifts in our experiments. We specifically focused our attention on areas of the protein that are of interest for drug design and/or biological function: the

active site, nearby loops associated with substrate binding, and the dimer interface.

First, the M^{PRO} active-site structure remains mostly consistent across our temperature series (Fig. S4). The catalytic amino acids are in very similar conformations across the temperatures. Additionally, a key active-site water molecule (known as H_2O_{cat}), which hydrogen bonds to His41 of the catalytic dyad and the side chains of His164 and Asp187 (both in the active site), remains in the same position across our structures (Fig. S4). It has been suggested (Kneller, Phillips, O'Neill, Jedrzejczak *et al.*, 2020) that this water may play the role of a third catalytic residue (in addition to the catalytic dyad of His41 and Cys145). As noted previously (Kneller, Phillips, O'Neill, Jedrzejczak *et al.*, 2020), H_2O_{cat} is not modeled in some cryogenic structures – but it is modeled in 87% (272/311) of the publicly available structures of SARS-CoV-2 M^{PRO} as of October 11, 2021 (the vast majority of which are cryogenic), and perhaps should have been modeled in others (Jaskolski *et al.*, 2021).

As with the active-site amino acids and H_2O_{cat} , a dimethyl sulfoxide (DMSO) molecule from the crystallization solution is ordered nearby in each structure in the multitemperature series (Fig. S4, left of each panel). Interestingly, however, this DMSO molecule is displaced by a water molecule in the high-humidity data set (298 K, 99.5% RH) [Fig. S4(f)], suggesting that the solvation distribution of the M^{PRO} active site is malleable. Similarly, another DMSO molecule in a distal region of the protein is ordered throughout the multitemperature series, but two waters and a new side-chain rotamer for Arg298 displace it in the high-humidity data set.

In addition to these solvent molecules, we observe an unanticipated feature in the active site in all of our data sets: an electron-density peak between the side chains of Cys145 and His41, which form the catalytic dyad (Figs. S4 and S5). We initially modeled a water molecule at this position, as in two previous apo structures: 7k3t Version 1.0 (the highest-resolution M^{PRO} structure available; apo state; Andi *et al.*, 2022) and 7jfq ('de-oxidized C145', no publication). However, the interatomic distances between a putative water oxygen and

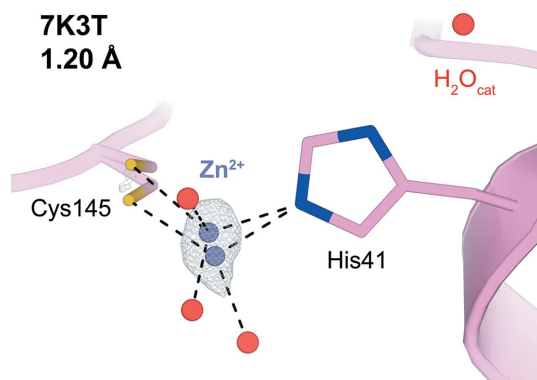


Figure 2
7k3t anomalous density map, contoured at 4σ . Anomalous density is only present in the asymmetric unit above 4σ in the vicinity of the active site (as shown here). Both Zn^{2+} alternate conformations modeled in 7k3t display tetrahedral coordination geometry, as shown with black dotted lines.

Table 2

Refinement statistics for *Phenix* ensemble models.

P_{TLS} and $w_{\text{X-ray}}$ are input parameters to *Phenix* ensemble refinement; the other input parameter (τ_x) was automatically determined (see *Methods* section).

Structure	100 K	240 K	277 K	298 K	298 K, 99.5% RH	310 K
PDB entry	7mhl	7mhm	7mhn	7mho	7mhp	7mhq
Resolution (Å)	1.55	1.53	2.19	1.88	2.00	1.96
P_{TLS}	0.8	0.8	0.8	0.8	0.8	0.8
$w_{\text{X-ray}}$	10.0	10.0	10.0	10.0	10.0	10.0
No. models in ensemble	54	43	45	75	28	36
R_{work}	0.1658	0.1575	0.1531	0.1499	0.1594	0.1705
R_{free}	0.2272	0.1967	0.2153	0.2083	0.2213	0.2348

the nearest atoms in Cys145 and His41 are relatively short, leading to steric clashes (Fig. S6), so we explored other possible explanations for this peak. Zn^{2+} binds tightly to M^{PRO} with 300 nM affinity (Panchariya *et al.* 2021), and when soaked into M^{PRO} crystals in previous studies (PDB entry 7dk1 and 7b83) [Fig. S9(b)], it was well ordered at our site of interest amidst the catalytic dyad. By contrast, we did not intentionally include Zn^{2+} at any stage, and Zn^{2+} is absent from almost all structures of M^{PRO} in the PDB aside from a select few structures for which it was intentionally included, arguing against its presence in our structures. Nonetheless, we considered the possibility that low levels of cellular Zn^{2+} serendipitously bound to our sample of M^{PRO} during expression and purification, and remained present during crystallization and X-ray data collection.

We therefore performed X-ray fluorescence (XRF) experiments on the original crystallization drops. The XRF results are consistent with the presence of Zn^{2+} (Fig. S7), but not other candidate metals, such as Ni^{2+} . Although we did not observe significant anomalous density at this site, this may be due to the fact that our diffraction data had been collected at a wavelength that does not perfectly align with the Zn^{2+} anomalous edge (see *Methods* section). We performed XRF many months after initial diffraction data collection, at which time the crystals no longer diffracted, so we could not collect new anomalous diffraction data at the Zn^{2+} anomalous edge for the crystals constituting our multitemperature series. Preparing a new batch of crystals to do so might have led to differences in the metal content, particularly given the absence of Zn^{2+} from the vast majority of structures of M^{PRO} . Instead, we re-examined the original diffraction data for the apo structure 7k3t, which – critically – were collected from the same batch of crystals as our multitemperature data sets reported here, and are of significantly higher resolution (1.20 Å). We observe a strong anomalous peak at the position in question for 7k3t, despite also having used an off-edge wavelength for Zn^{2+} (Fig. 2). A new 7k3t Version 2.0 model is therefore deposited in the PDB with anomalous data included and Zn^{2+} instead of H_2O modeled, and is described elsewhere (Andi *et al.*, 2022).

In response to these observations, we have modeled Zn^{2+} at partial occupancy (0.20–0.31) in each of our multitemperature structures (Fig. S4). These refined crystallographic occu-

pancies are similar and imply a small energy difference (Davis *et al.*, 2006) of <0.5 kT. The resulting structures have excellent Zn^{2+} -binding geometry and the resulting maps are free of large difference peaks. Interestingly, in our temperature series, the position of Zn^{2+} varies across temperatures by nearly 1 Å, which is in excess of the estimated coordinate error ranging from ± 0.08 to ± 0.32 Å for our structures (calculated using the Diffraction Precision Index online server; Kumar *et al.*, 2015),

along an approximately linear swath (Fig. S8). This result is in line with the presence of alternate conformations displaced by over 0.7 Å along a similar vector for the Zn^{2+} in the higher-resolution 7k3t Version 2.0 [Fig. S9(a)], and also coincides with a swath of O atoms from a series of covalent ligands [Fig. S8(c)].

Beyond the active site, we turned our attention to the nearby P5 binding pocket, specifically the loop composed of

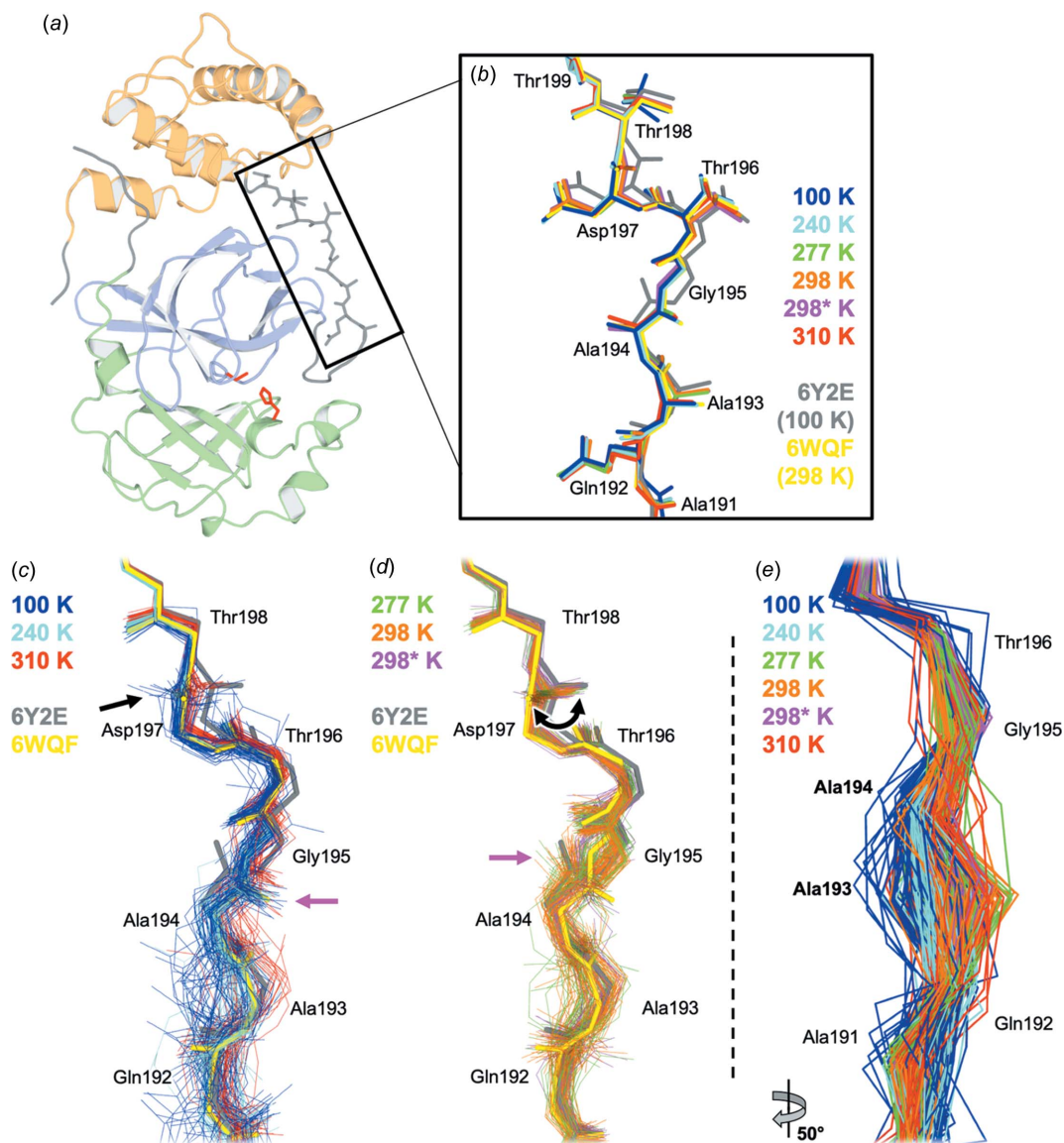


Figure 3

Complex temperature dependence of residues 192–198 in the P5 binding pocket. (a) M^{pro} monomer from a cryogenic structure, colored by domain: domain I, residues 8–101, pale green; domain II, residues 102–184, pale blue; domain III, residues 201–303, pale orange. Catalytic dyad residues Cys145 and His41 are shown as sticks (red). Terminal residues are shown in dark gray. P5 binding-pocket linker loop (residues 190–200) shown in dark gray and as sticks (black box). (b) Our new multitemperature structures all have a single backbone conformation for this linker loop region. Regardless of temperature, they all match a similar backbone conformation to the room-temperature 6wqf model (yellow), and not the cryogenic 6y2e model (gray) (Kneller, Phillips, O’Neill, Jedrzejczak *et al.*, 2020) (298* K = 298 K, 99.5% relative humidity). (c)–(e) *Phenix* ensemble refinement models based on our multitemperature data sets reveal a complex pattern of flexibility that was ‘hidden’ in part (b). (c) For some conditions (100 K, blue; 240 K, cyan; 310 K, red), the ensemble models generally match 6wqf, albeit with variability around the average conformation. For the Ala194–Gly195 peptide (pink arrow), these ensembles match 6wqf. For the Asp197–Thr198 peptide (black arrow), they match 6wqf. (d) For other conditions (277 K, green; 298 K, orange; 298* K, magenta), the ensemble models exhibit shifts away from 6wqf and toward 6y2e. For the Ala194–Gly195 peptide, these ensembles match 6y2e (pink arrow) instead of 6wqf. For the Asp197–Thr198 peptide, they adopt a swath of orientations (black curved arrow) bridging 6wqf and 6y2e. (e) A $\sim 50^\circ$ counterclockwise-rotated view of all multitemperature ensemble models, shown as $C\alpha$ atoms only, illustrates the conformational clustering of the 100–240 K ensembles around residues 193–194 in the P5 binding pocket (bold text), while the 277–310 K ensembles occupy a broader swath of positions within this region.

residues 192–198 (Fig. 3). Previously, the first report of a room-temperature structure of M^{Pro}, which was in the apo form (PDB entry 6wqf) (Kneller, Phillips, O'Neill, Jedrzejczak *et al.*, 2020), noted that this loop adopted a different conformation than in a prior 100 K apo structure (PDB entry 6y2e) (Zhang *et al.*, 2020), including rotated peptide orientations for Ala194–Gly195 and Asp197–Thr198. However, all of the structures in our multitemperature series, including at lower temperatures (100 and 240 K), have a single backbone conformation in this region that matches that of 6wqf [Fig. 3(b)].

In addition, other apo cryogenic structures, including one at high (1.2 Å) resolution (PDB entry 7k3t), also match the 6wqf backbone conformation. All of these structures (6wqf, 6y2e, 7k3t, and our multitemperature series) derive from the same crystal form (Table 1). Thus, it appears that the different loop conformation adopted in 6y2e is not driven by temperature (Kneller, Phillips, O'Neill, Jedrzejczak *et al.*, 2020), nor by ligand binding or crystal-lattice effects, but rather by some other aspect of the crystallization details or sample-handling conditions – including, perhaps, idiosyncratic effects of crystal

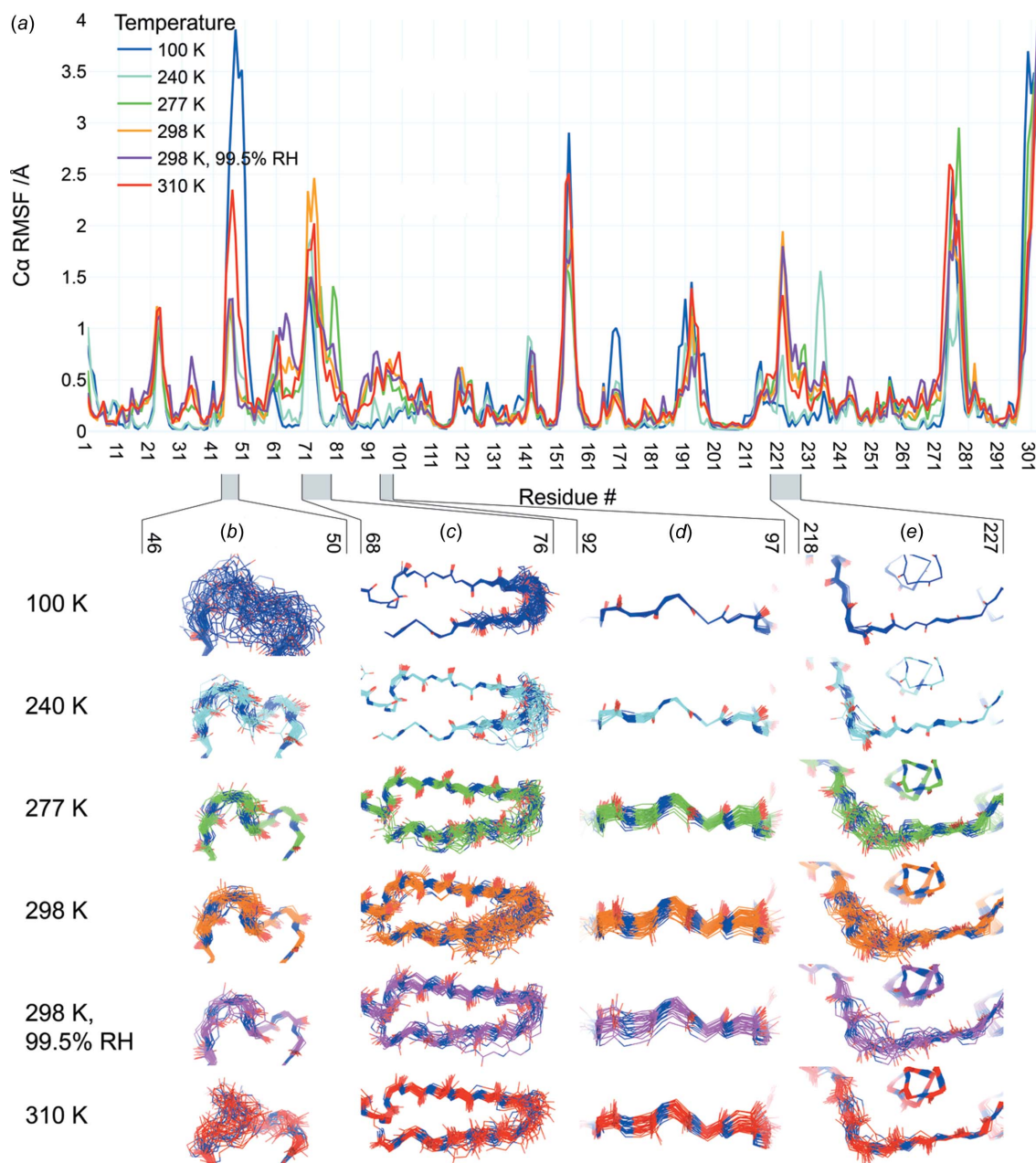


Figure 4 Backbone structural variability of ensemble models along the M^{Pro} sequence as a function of temperature. (a) RMSF of the backbone C α -atom positions is plotted *versus* residue number for each of the different structures in our multitemperature series (colors in legend). RMSF spikes at the N-terminus, C-terminus, and β -turn 153–157 (in contact with the C-terminus) in the ensemble models are truncated in this plot, and should be interpreted with caution. (b)–(e) Backbone structures from ensemble refinement are shown for regions coinciding with temperature-dependent RMSF peaks. The refined single structure is shown as a cartoon, while atoms in the backbone of ensemble models are shown as lines.

cryocooling (Halle, 2004; Keedy *et al.*, 2014). Our conclusion here is also supported by a recent retrospective analysis of existing structures (Jaskolski *et al.*, 2021).

2.4. Crystallographic ensemble models reveal distinct backbone conformational heterogeneity

We next aimed to complement this analysis of our manually built multiconformer models with a more automated and explicitly unbiased approach to modeling flexibility that can handle larger-scale backbone flexibility such as loop motions. Therefore, we turned to *Phenix* ensemble refinement, which uses molecular dynamics simulations with time-averaged restraints to crystallographic data (Burnley *et al.*, 2012). *Phenix* ensemble models have been used fruitfully for many applications (Woldeyes *et al.*, 2014), including exploring the effects of temperature on protein crystals (Keedy *et al.*, 2014), assessing the conformational plasticity of peptide–MHC interactions (Fodor *et al.*, 2018), and rational protein design (Broom *et al.*, 2020). After a scan of parameter space (see *Methods* section), we created one ensemble model per temperature, each of which contains 28 to 75 constituent models (Table 2). Compared to the multiconformer models, the

ensemble models fit the experimental data equally well or better based on R_{free} , albeit with slightly wider $R_{\text{free}}-R_{\text{work}}$ gaps (Table 2 *versus* Table 1).

Using these ensemble models, we re-examined the P5 binding pocket loop mentioned above. The 100, 240, and 310 K ensemble models are similar to the previous ‘room-temperature’ structure 6wqf, with mostly the same peptide orientation for Ala194–Gly195 and Asp197–Thr198 [Fig. 3(c)]. By contrast, the 277, 298, and 298 K (99.5% RH) ensemble models mostly match the flipped Ala194–Gly195 peptide orientation from the previous cryogenic structure 6y2e, and sample a swath of conformations for Asp197–Thr198 that span 6wqf and 6y2e [Fig. 3(d)]. This distinction between peptide conformations that match 6wqf *versus* 6y2e is not simply a by-product of resolution, as 298 K is higher resolution than 310 K. More broadly, our ensembles reveal that the backbone of residues 192–195 occupies a distinct clustered conformation at the lower temperatures of 100–240 K, while sampling a comprehensive swath of positions at the higher temperatures of 277–310 K [Fig. 3(e)]. Taken together, these results suggest that this region of M^{pro} has a complex relationship between temperature and conformational heterogeneity.

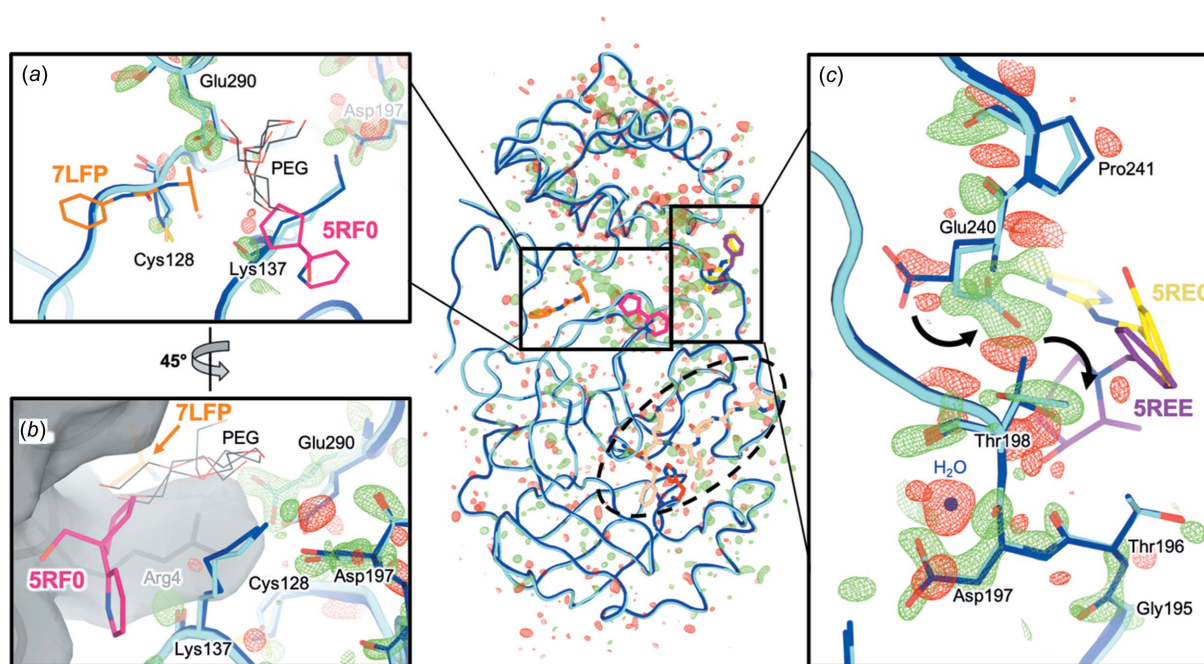


Figure 5

$F_o - F_o$ difference maps reveal local conformational shifts connecting the active site, interdomain interface, and dimer interface. Center: overview of the isomorphous $F_o - F_o$ difference electron-density map at $\pm 3\sigma$ (green–red mesh) for the 240 K data set (cyan) minus the 100 K data set (dark blue) (see Fig. S10 for $F_o - F_o$ maps for all temperatures). Ligands from cocrystal structures are shown at the active site (dashed oval) (pale orange, 6lu7), interdomain interface (purple, 5ree; yellow, 5rec), and dimer interface (orange, 7lfp; pink, 5rf0). (a) Glu290 switches from one side-chain rotamer at 100 K to two alternate rotamers at 240 K. Glu290 is spatially adjacent to Cys128, which switches from two alternate rotamers at 100 and 240 K to a single rotamer at 277 K and above in our multiconformer models; the alternate rotamer occupancy is lower at 240 K, consistent with its positive $F_o - F_o$ peak (see Fig. S12). These residues are near two ligands from separate crystallographic screens (7lfp and 5rf0), as well as many ordered PEG molecules from the crystallization cocktails of various structures (7kvr, 7kvl, 7kfi, and 7lfe). (b) An $\sim 45^\circ$ -rotated view relative to part (a) shows that these two ligands bind at the dimer interface of the biological monomer, constituted in the crystal from a symmetry-related protomer (gray surface). This interface also includes the Asp197 region (right). (c) Thr198 switches from two alternate side-chain rotamers at 100 K to a single rotamer at 240 K, while Glu240 – located across the interdomain interface – changes side-chain rotamer (curved arrows), with additional effects on the adjacent backbone of Pro241. In the other direction from Asp197 (down in this view), other residues in the P5 substrate-binding pocket loop (Fig. 3) undergo conformational adjustments en route to the active site. Meanwhile, an interacting water molecule at 100 K (blue sphere) becomes displaced at 240 K, and is correspondingly absent in that model.

Beyond just the P5 loop, we also examined other regions with elevated and/or temperature-dependent ensemble C α r.m.s. fluctuation (RMSF) [Fig. 4(a)] that were not previously noted as being temperature dependent. These regions segregate into different categories with distinct temperature dependence.

First, some regions display a generally positive correlation between backbone structural variability and diffraction experiment temperature. For example, in residues 68–76 [Fig. 4(c)], conformational diversity is restricted to the β -hairpin at 100 and 240 K, but appears to spread further down the β -strands at higher temperatures. In another case, residues 92–97 [Fig. 4(d)] and 218–227 [Fig. 4(e)] are highly ordered at 100 and 240 K, but mobile at warmer temperatures. Interestingly, although these two regions (92–97 and 218–227) are isolated from each other in the monomer and the biologically relevant dimer, together they form a contiguous patch with 68–76 in the crystal lattice. Finally, we observe one region with an atypical relation between backbone variability and temperature: the short 3_{10} helix at residues 46–51 [Fig. 4(b)]. This region abuts the P5 substrate-binding loop composed of residues 192–198 with its complex temperature dependence (Fig. 3); together these two regions form one side of the active-site pocket [Fig. 1(b)].

2.5. A network of coupled conformational heterogeneity bridges the active site, substrate pocket, interdomain interface, and dimer interface

To complement the model-centric approaches above, we also looked for temperature-dependent conformational effects using an approach that is more directly data-driven: isomorphous $F_o - F_c$ difference electron-density maps. We computed $F_o - F_c$ difference maps for each temperature *versus* 100 K, and looked for patterns in terms of spatial colocalization of difference peaks. The global results confirm that the protein structure remains similar overall, with a smattering of difference peaks throughout the monomer asymmetric unit (Fig. S10). However, within those difference peaks lies a provocative stretch of difference features spanning the dimer interface, the interface between domain I and domain II of the monomer, and the edge of the P5 substrate-binding pocket (Fig. 5). These difference features may be somewhat resolution dependent, as they are least pronounced for 277 K (2.19 Å) and most pronounced for 240 K (1.53 Å), but their distribution across M^{PRO} is qualitatively similar across temperatures. These features are not an artifact of diffraction anisotropy (Fig. S11).

A closer examination of the models in the vicinity of these difference features reveals what appears to be a series of correlated conformational motions keyed to temperature change. For example, $F_o - F_c$ density shows that Glu290 shifts from a single side-chain rotamer at 100 K to two alternate rotamers with partial occupancies at 240 K [Fig. 5(a)]; this second rotamer seen at 240 K then remains as a single full-occupancy conformation for all higher temperatures. Spatially adjacent to Glu290, Cys128 gradually shifts from two alternate rotamers at 100 K toward a single rotamer at higher temper-

atures; at the intermediate temperature of 240 K, the alternate rotamer still exists but has lower occupancy than at 100 K (Fig. S12), which is consistent with the presence of a positive 240–100 K $F_o - F_c$ peak [Fig. 5(a)]. Both Glu290 and Cys128 interact with a symmetry-related Arg4 across the biological dimer interface [Fig. 5(b)]. Interestingly, two small-molecule fragments from recent crystallographic screens (Douangmath *et al.*, 2020; Noske *et al.*, 2021) bind at this area of the dimer interface [Figs. 5(a) and 5(b)]. Moreover, ordered polyethylene glycol (PEG) molecules from several previous structures [PDB entries 7kvr, 7kvl, 7kfi, and 7lfe; Figs. 5(a) and 5(b)] illustrate the potential for future ligand design efforts to ‘grow’ from one of these initial fragment hits (5rf0) toward the mobile Glu290 and Cys128. This observation reinforces the idea that molecules from crystallization solutions, such as glycols, can reveal useful features like cryptic binding pockets (Bansia *et al.*, 2021).

Glu290 is connected to another interesting residue, Asp197, *via* a hydrogen-bond network with only one intervening side chain (Arg131). Within this vicinity, an interacting water molecule is liberated, and an adjacent residue, Thr198, shifts from two alternate side-chain rotamers to just one [Fig. 5(c)]. The Thr198 motion is linked to a conformational re-ordering for the nearby Glu240 side chain and Pro241 backbone, thus establishing a possible means for allosteric communication across the interdomain interface. In the opposite direction from Asp197, other adjacent residues experience changes in ordering per $F_o - F_c$ peaks; these residues together form the 192–198 loop of the functionally important and mobile P5 pocket (Fig. 3) leading toward the active site.

Overall, these observations describe a series of conformational motions that bridge the dimer interface, interdomain interface, substrate-binding pocket, and active site (Fig. 5, center, boxes and oval). In this work, temperature is the perturbation/effector – but our results raise the enticing possibility that future small molecules could be used to allosterically perturb this network, thereby modulating enzyme dimerization and/or catalysis.

3. Discussion

Our crystal structures of unliganded SARS-CoV-2 M^{PRO} at variable temperature and humidity paint a picture of a complex protein conformational landscape. The structure of M^{PRO} does not change linearly with temperature; rather, there is a global transition between roughly <240 and >277 K [Figs. 1(d) and S2]. This 240–277 K transition regime for M^{PRO} does not coincide with the 180–220 K glass transition or dynamical transition threshold seen previously for other systems such as CypA (Keedy *et al.*, 2015), suggesting protein-to-protein variability. More locally in M^{PRO}, as temperature increases, different regions experience distinct types of changes to conformational heterogeneity (Fig. 4), in line with previous multitemperature studies of other proteins (Keedy *et al.*, 2014). These effects are not limited to surface-exposed side chains as one might naïvely expect, but rather encompass motions of buried side chains (Fig. 5) and many backbone

regions (Figs. 3 and 4). Our results here for M^{PRO}, as well as a large body of previous literature for other systems, refute the assertion that X-ray crystallography under ‘unusual experimental conditions’ like variable temperature is not useful for understanding proteins (Jaskolski *et al.*, 2021). By contrast, our work is in line with computational analyses of *B* factors suggesting that different alternate conformations for M^{PRO} (and other systems) can be accessed by varying temperatures and/or the crystal lattice (Pearce & Gros, 2021).

Our structures contain serendipitously bound low-occupancy Zn²⁺ at the site of chemistry, presumably from the bacterial cells used for protein expression. It should be noted that the presence of Zn²⁺ in the active site of our structures may bias the temperature response and complicate efforts to exploit these structures for structure-based drug design. It is unclear why this Zn²⁺ is absent in most previous structures of M^{PRO}. Notably, recent structures of an acyl–enzyme intermediate structure (PDB entry 7khp) and a C145A mutant product-bound structure (PDB entry 7joy) of M^{PRO} include a nearby water, ~1.5 Å away but aligned with our approximately collinear multitemperature Zn²⁺ swath, which the authors suggested may play a role as a deacylating nucleophile (Lee *et al.*, 2020). Questions about the energetic landscape of this catalytic dyad region and its relation to function could be explored in parallel with other experiments, such as variable pH to probe Cys145 oxidation and reactivity (Kneller, Phillips, O’Neill, Tan *et al.*, 2020), and neutron crystallography to reveal a zwitterionic state of the catalytic dyad (Kneller, Phillips, Weiss *et al.*, 2020), although questions remain about the interpretation of such data (Jaskolski *et al.*, 2021).

High relative humidity during data collection does not dramatically affect our structures [Figs. 1(*d*) and S2]. However, it does alter the solvation shell in the active site (Fig. S4, bottom left) and elsewhere. Displaceable waters could potentially be exploited to design high-affinity small-molecule inhibitors, particularly when guided by water thermodynamics maps from simulations, as are available for M^{PRO} and other SARS-CoV-2 proteins (Olson *et al.*, 2020). More broadly, this result hints at the utility of humidity as an experimental variable in crystallography (Kiefersauer *et al.*, 2000; Sanchez-Weatherby *et al.*, 2009) for exploring solvent slaving to solvent energetics in ligand binding (Darby *et al.*, 2019), protein dynamics (Lewandowski *et al.*, 2015), and other functionally relevant phenomena.

Phenix ensemble models (Burnley *et al.*, 2012) refined from our X-ray data sets helped us to illuminate temperature-dependent differences in conformational heterogeneity in certain areas of M^{PRO} (Figs. 3 and 4) that were concealed by more traditional model types (Babcock *et al.*, 2018). Despite its utility in this and other work, there is significant potential for improvement of the ensemble refinement methodology through, for example, integration of more sophisticated molecular mechanics force fields like Amber (Moriarty *et al.*, 2020) into the molecular dynamics component (Burnley *et al.*, 2012) to improve ensemble model geometry, or more sophisticated treatments of translation–libration–screw (TLS) groups to isolate interesting local conformational hetero-

geneity (Ploscariu *et al.*, 2021). Although it was also beyond the scope of this study, ensemble models may reveal alternate conformational substates that are important for the catalytic cycle, which could be fruitfully targeted by small molecules for antiviral drug design.

Finally, our results emphasize the allure of allosteric inhibition of M^{PRO} as an alternative therapeutic strategy. Allosteric inhibitors hold the potential to target unutilized sites, though they can face mutational escape by the protein target (Lu *et al.*, 2020). Our structures illustrate apparently coupled conformational motions that bridge the active site, substrate-binding pocket, interdomain interface, and parts of the broad dimer interface (Figs. 4 and 5). This is particularly noteworthy since M^{PRO} must dimerize to become an active enzyme (Fan *et al.*, 2004; Goyal & Goyal, 2020). Interdomain flexing has also been observed, even in crystals (Jaskolski *et al.*, 2021). The intramolecular network we describe includes several sites that are distal from the active site, one of which is highlighted by Glu240 difference density [Fig. 5(*c*)] corresponding to a temperature-dependent rotamer flip, with this site having already been characterized as ligandable by recent crystallographic screens of pre-existing drug molecules (Günther *et al.*, 2021) and small-molecule fragments (Douangamath *et al.*, 2020) (Fig. 5). Some new M^{PRO} ligands have been shown by mass spectrometry to disrupt the M^{PRO} dimer and allosterically inhibit catalysis, albeit weakly thus far (El-Baba *et al.*, 2020), illustrating the potential of an allosteric strategy. As a complementary structure-based approach to current experiments on the dimeric crystal form of M^{PRO}, future experiments could exploit mutations of the dimer interface to stabilize an inactive monomer, thus capturing a new structural target for crystallographic and solution screening for allosteric inhibitors that block dimerization. Ultimately, the present study offers insights into fundamental aspects of protein structural biophysics, and may also help pave the way for new efforts toward allosteric modulation of M^{PRO} as a strategy for coronavirus drug design.

4. Methods

4.1. Cloning, expression, and purification

Full details of the cloning, expression, and purification are reported elsewhere (Andi *et al.*, 2022). Briefly, the codon-optimized synthetic gene of full-length M^{PRO} from SARS-CoV-2 was cloned into the pET29b vector. The cloned M^{PRO} with C-terminal 6x histidine tag was expressed in *E. coli* using an auto-induction procedure (Studier, 2005). Cells were harvested, lysed using bacterial protein extraction agents (B-PER, ThermoFisher Scientific) in the presence of lysozyme, and purified with nickel-affinity chromatography followed by size-exclusion chromatography. The histidine tag was cleaved by human rhinovirus (HRV) 3C protease (AcroBIOSYSTEMS) and further purified by reverse nickel-affinity chromatography. The purified protein was then dialysed overnight at 4°C against 30 mM HEPES pH 7.4, 200 mM NaCl, 1 mM TCEP. Finally, the protein was concentrated to ~7 mg ml⁻¹ and either used for crystallization or stored at -80°C.

4.2. Crystallization

Plate-like crystals ranging from ~ 100 – $400\ \mu\text{m}$ along the longest axis (~ 5 – $10\ \mu\text{m}$ along the shortest axis) were grown *via* sitting-drop vapor diffusion. The crystals grew in ‘flower-like’ clusters (Fig. S13). After mixing a 1:1 ratio of $\sim 7\ \text{mg ml}^{-1}$ M^{Pro} with a solution of 22% PEG 4000, 100 mM HEPES pH 7.0, 3–5% DMSO and incubating at a temperature of $\sim 298\ \text{K}$, crystals were seen after 2–6 d.

4.3. Crystal harvesting and X-ray data collection

Individual crystals were harvested using $10\ \mu\text{m}$ MicroMesh loops (MiTeGen). For cryogenic temperature, crystals were cryocooled by the traditional practice of plunging into liquid nitrogen. For non-cryogenic temperatures at ambient humidity, crystals were coated with Paratone-N oil, then mounted on the goniometer for data collection. Data sets were also collected for crystals coated with Paratone-N oil and additionally enclosed in MicroRT capillaries (MiTeGen), but no differences were observed relative to Paratone-N oil only. For high humidity, crystals were not coated with Paratone-N oil, but were enclosed in MicroRT capillaries for the short transit to the goniometer, then removed once a humid air flow was established on the goniometer; this ensured the crystal was always maintained at high humidity after leaving the crystallization drop. Each crystal was equilibrated on the goniometer for 10–20 min, which is more than sufficient to reach stable conditions.

X-ray diffraction data were collected at the National Synchrotron Light Source II (NSLS-II) beamline 17-ID-2 (FMX) (Schneider *et al.*, 2021) using an X-ray beam of energy 12.66 keV, corresponding to a wavelength of $0.9793\ \text{\AA}$; a horizontal-bounce Si111 double-crystal monochromator; and an EIGER X 16M pixel array detector (Dectris). The temperature at the sample goniometer was controlled using a Cryostream 800 (Oxford Cryosystems). For the 298 K, 99.5% relative humidity (RH) data set, RH was controlled with an HC-LAB Humidity Controller (Arinax). Ambient temperature was measured to be $\sim 298\ \text{K}$ and ambient humidity was measured to be 36.7%. A new crystal was used for each data set. Helical/vector data collection was used to traverse the length of each crystal, with a beam size of $10 \times 10\ \mu\text{m}$. Using *RADDOSE-3D* (Bury *et al.*, 2018), we estimated the average diffraction-weighted dose (ADWD) for our data sets to be 242 kGy for 100 K, 532 kGy for 240 K, 397 kGy for 277 K, 137 kGy for 298 K, 182 kGy for 298 K (99.5% RH), and 176 kGy for 310 K. All of these ADWD values are at or below the estimated room-temperature limit of about 400 kGy (Fischer, 2021) for our higher temperatures, although this limit is generally system dependent. The ADWD for 240 K is above the room-temperature limit, but such lower temperatures have higher dose tolerance. Additionally, there was no evidence of global radiation damage from R_d plots (Fig. S1), and local/specific radiation damage did not appreciably accrue during the course of each single-crystal data collection, as indicated by $2F_o - F_c$ electron-density maps around carboxyl groups (not shown).

For independent verification of the presence of metals in the crystal samples, we collected X-ray fluorescence spectra and performed edge scans. For fluorescence spectra data collection, the radiation emitted and scattered from the crystal was detected with an energy-dispersive Si drift detector (Ketek VIAMP KC), in a configuration to collect radiation scattered or emitted in a horizontal direction perpendicular to the incoming X-ray beam. For energy edge scans, the incoming photon energy was scanned across the absorption edge of the scatterer under investigation while detecting the integrated intensity of photons in a region of interest around the expected associated X-ray fluorescence emission line.

4.4. X-ray data reduction and modeling

The data reduction pipeline *fast_dp* (Winter & McAuley, 2011) was initially used for bulk data reduction during the beamtime, with selected data reprocessed using the *xia2 DIALS* (Winter *et al.*, 2018) and *xia2 3dii* (*XDS* and *XSCALE*) pipelines (Kabsch, 2010), with *xia2 3dii* (*XDS* and *XSCALE*) also being used for the generation of R_d statistics (Diederichs, 2006) (Fig. S1). Resolution cut-offs were chosen based on $CC_{1/2}$ being $> \sim 0.3$ in order to include data at lower signal levels that improve the model (Karplus & Diederichs, 2012), in combination with high overall and outer-shell completeness (Afonine *et al.*, 2012; Arkhipova *et al.*, 2017). Molecular replacement for each data set was performed *via Phaser-MR* from the *Phenix* software suite, using PDB entry 6yb7 as a search model. *Phenix AutoBuild* (Terwilliger *et al.*, 2008) was used for initial model building and refinement, with subsequent iterative refinements performed using *phenix.refine* (Afonine *et al.*, 2012) and *Coot* (Emsley & Cowtan, 2004). After a few initial rounds of refinements, H atoms were added using *phenix.ready_set* [*Reduce* (Word *et al.*, 1999) and *eLBOW* (Moriarty *et al.*, 2009)]. For refinement of each data set, X-ray/stereochemistry weight and X-ray/ADP weight were refined and optimized. Geometric and protein statistics of the final models were evaluated *via MolProbity* (Chen *et al.*, 2010; Williams *et al.*, 2018) and the JCSG–QC check server (<https://smb.slac.stanford.edu/jcsg/QC/>). Data collection and refinement statistics are shown in Table 1.

Crystallographic ensemble models were generated using *phenix.ensemble_refinement* (Burnley *et al.*, 2012) in Version 1.18.2-3874 of *Phenix*. Alternate conformations were first removed from the multiconformer models, and H atoms were (re)added using *phenix.ready_set*. Next, a *phenix.ensemble_refinement* grid search was performed by repeating the simulation with four values of p_{TLS} (1.0, 0.9, 0.8, 0.6) and three values of $w_{\text{ray_coupled_tbath_offset}}$ (10, 5, 2.5), and using a *random_seed* value of 2679941. τ_x was set automatically according to the high-resolution limit of the data set. From this grid, we present the analysis of the set of ensemble models that has the lowest mean R_{free} : $p_{\text{TLS}} = 0.8$ and $w_{\text{ray_coupled_tbath_offset}} = 10.0$. Although we chose one ensemble model per data set, the trends we describe in this report were generally consistent across alternative ensemble models with different parameter choices. In line with this consistency, when

comparing the alternative ensemble models we considered, the R_{free} values for any particular crystal differed by at most 2.8% and R_{work} values by at most 1.6%. Refinement statistics are shown in Table 2.

For $F_o - F_o$ isomorphous difference map analysis, the *phenix.fobs_minus_fobs_map* executable in the *Phenix* software suite was used. This program performs internal scaling of the two data sets to each other. Each elevated temperature was compared to 100 K. The 100 K multiconformer model was used for phasing for each difference map. The effects of diffraction anisotropy were assessed using the *STARANISO* server (Tickle *et al.*, 2018) to perform an anisotropic cut-off of merged intensity data for all temperatures. *STARANISO* data sets were compared to our multitemperature series in *Coot* and using *phenix.fobs_minus_fobs* (Fig. S11) to survey whether diffraction anisotropy gives rise to variations in difference density. For solvent content analysis, *rwcontents* (Version 7.1.009) from the *CCP4* suite (Winn *et al.*, 2011) was used.

5. Accession numbers and data availability

Models and structure factors are available in the Protein Data Bank under the following PDB entry accession codes (see also Tables 1 and 2): 7mhf, 7mhg, 7mhh, 7mhi, 7mhj, and 7mhk for multiconformer models, and 7mhl, 7mhm, 7mhn, 7mho, 7mhp, and 7mhq for ensemble models. New versions (Version 2.0) of each of these structures were deposited after modeling Zn^{2+} instead of H_2O in the active site.

Diffraction data are available at the Integrated Resource for Reproducibility in Macromolecular Crystallography (<https://proteindiffraction.org>) under the following DOIs: 10.18430/m37mhf, 10.18430/m37mhg, 10.18430/m37mhh, 10.18430/m37mhi, 10.18430/m37mhj, and 10.18430/m37mhk.

6. Glossary

$F_o - F_o$ = isomorphous difference electron-density map.
 COVID-19 = coronavirus disease 2019. SARS-CoV-2 = severe acute respiratory syndrome coronavirus 2. M^{pro} = SARS-CoV-2 coronavirus main protease.

Acknowledgements

We thank our reviewers for providing useful feedback that improved the manuscript, Jean Jakoncic for consultation on anomalous data processing, and Michael Thompson for helpful discussions. This research was supported by the DOE Office of Science through the National Virtual Biotechnology Laboratory (NVBL) with funding from the Coronavirus CARES Act and additional funding was provided by Brookhaven National Laboratory (BNL) for research on COVID-19 (LDRD 20-042). This research used beamline FMX (17-ID-2) of the National Synchrotron Light Source II, a US Department of Energy (DOE) Office of Science User Facility operated for the DOE Office of Science by Brookhaven National Laboratory under contract No. DE-SC0012704. The Center

for BioMolecular Structure (CBMS) is primarily supported by the National Institutes of Health, National Institute of General Medical Sciences (NIGMS) through a Center Core P30 Grant (P30GM133893), and by the DOE Office of Biological and Environmental Research (KP1605010). The authors declare no competing interests.

Funding information

Funding for this research was provided by: National Institutes of Health (grant No. R35 GM133769 to DAK); Brookhaven National Laboratory (award No. LDRD 20-042).

References

- Afonine, P. V., Grosse-Kunstleve, R. W., Echols, N., Headd, J. J., Moriarty, N. W., Mustyakimov, M., Terwilliger, T. C., Urzhumtsev, A., Zwart, P. H. & Adams, P. D. (2012). *Acta Cryst.* **D68**, 352–367.
- Andi, B., Kumaran, D., Kreitler, D. F., Soares, A. S., Keereetawee, J., Jakoncic, J., Lazo, E. O., Shi, W., Fuchs, M. R., Sweet, R. M., Shanklin, J., Adams, P. D., Schmidt, J. G., Head, M. S. & McSweeney, S. (2022). *Sci. Rep.* **12**, 12197.
- Arkhipova, V., Guskov, A. & Slotboom, D. (2017). *J. Gen. Physiol.* **149**, 1091–1103.
- Atakisi, H., Moreau, D. W. & Thorne, R. E. (2018). *Acta Cryst.* **D74**, 264–278.
- Babcock, N. S., Keedy, D. A., Fraser, J. S. & Sivak, D. A. (2018). *bioRxiv*. doi: <https://doi.org/10.1101/448795>.
- Bansia, H., Mahanta, P., Yennawar, N. H. & Ramakumar, S. (2021). *J. Chem. Inf. Model.* **61**, 1322–1333.
- Baum, A., Ajithdoss, D., Copin, R., Zhou, A., Lanza, K., Negron, N., Ni, M., Wei, Y., Mohammadi, K., Musser, B., Atwal, G. S., Oyejide, A., Goez-Gazi, Y., Dutton, J., Clemmons, E., Staples, H. M., Bartley, C., Klaffke, B., Alfson, K., Gazi, M., Gonzalez, O., Dick, E. Jr, Carrion, R. Jr, Pessaint, L., Porto, M., Cook, A., Brown, R., Ali, V., Greenhouse, J., Taylor, T., Andersen, H., Lewis, M. G., Stahl, N., Murphy, A. J., Yancopoulos, G. D. & Kyratsous, C. A. (2020). *Science*, **370**, 1110–1115.
- Beigel, J. H., Tomashek, K. M., Dodd, L. E., Mehta, A. K., Zingman, B. S., Kalil, A. C., Hohmann, E., Chu, H. Y., Luetkemeyer, A., Kline, S., Lopez de Castilla, D., Finberg, R. W., Dierberg, K., Tapson, V., Hsieh, L., Patterson, T. F., Paredes, R., Sweeney, D. A., Short, W. R., Touloumi, G., Lye, D. C., Ohmagari, N., Oh, M.-D., Ruiz-Palacios, G. M., Benfield, T., Fätkenheuer, G., Kortepeter, M. G., Atmar, R. L., Creech, C. B., Lundgren, J., Babiker, A. G., Pett, S., Neaton, J. D., Burgess, T. H., Bonnett, T., Green, M., Makowski, M., Osinusi, A., Nayak, S., Lane, H. C. & ACTT-1 Study Group Members, (2020). *N. Engl. J. Med.* **383**, 1813–1826.
- Berman, H. M., Westbrook, J., Feng, Z., Gilliland, G., Bhat, T. N., Weissig, H., Shindyalov, I. N. & Bourne, P. E. (2000). *Nucleic Acids Res.* **28**, 235–242.
- Boras, B., Jones, R. M., Anson, B. J., Arenson, D., Aschenbrenner, L., Bakowski, M. A., Beutler, N., Binder, J., Chen, E., Eng, H., Hammond, H., Hammond, J., Haupt, R. E., Hoffman, R., Kadar, E. P., Kania, R., Kimoto, E., Kirkpatrick, M. G., Lanyon, L., Lendy, E. K., Lillis, J. R., Logue, J., Luthra, S. A., Ma, C., Mason, S. W., McGrath, M. E., Noell, S., Scott Obach, R., O'Brien, M. N., O'Connor, R., Ogilvie, K., Owen, D., Pettersson, M., Reese, M. R., Rogers, T. F., Rossulek, M. I., Sathish, J. G., Shirai, N., Steppan, C., Ticehurst, M., Updyke, L. W., Weston, S., Zhu, Y., Wang, J., Chatterjee, A. K., Mesezar, A. D., Frieman, M. B., Anderson, A. S. & Allerton, C. (2021). In *Discovery of a Novel Inhibitor of Coronavirus 3CL Protease for the Potential Treatment of COVID-19*. Cold Spring Harbor Laboratory.

- Broom, A., Rakotoharisoa, R. V., Thompson, M. C., Zarifi, N., Nguyen, E., Mukhametzhanov, N., Liu, L., Fraser, J. S. & Chica, R. A. (2020). *Nat. Commun.* **11**, 4808.
- Burnley, B. T., Afonine, P. V., Adams, P. D. & Gros, P. (2012). *eLife*, **1**, e00311.
- Bury, C. S., Brooks-Bartlett, J. C., Walsh, S. P. & Garman, E. F. (2018). *Protein Sci.* **27**, 217–228.
- Chen, V. B., Arendall, W. B., Headd, J. J., Keedy, D. A., Immormino, R. M., Kapral, G. J., Murray, L. W., Richardson, J. S. & Richardson, D. C. (2010). *Acta Cryst. D* **66**, 12–21.
- Chodera, J., Lee, A. A., London, N. & von Delft, F. (2020). *Nat. Chem.* **12**, 581.
- Darby, J. F., Hopkins, A. P., Shimizu, S., Roberts, S. M., Brannigan, J. A., Turkenburg, J. P., Thomas, G. H., Hubbard, R. E. & Fischer, M. (2019). *J. Am. Chem. Soc.* **141**, 15818–15826.
- Davis, I. W., Arendall, W. B. III, Richardson, D. C. & Richardson, J. S. (2006). *Structure*, **14**, 265–274.
- Diederichs, K. (2006). *Acta Cryst. D* **62**, 96–101.
- Douangamath, A., Fearon, D., Gehrtz, P., Krojer, T., Lukacik, P., Owen, C. D., Resnick, E., Strain-Damerell, C., Aimon, A., Ábrányi-Balogh, P., Brandão-Neto, J., Carbery, A., Davison, G., Dias, A., Downes, T. D., Dunnett, L., Fairhead, M., Firth, J. D., Jones, S. P., Keeley, A., Keserü, G. M., Klein, H. F., Martin, M. P., Noble, M. E. M., O'Brien, P., Powell, A., Reddi, R. N., Skyner, R., Snee, M., Waring, M. J., Wild, C., London, N., von Delft, F. & Walsh, M. A. (2020). *Nat. Commun.* **11**, 5047.
- El-Baba, T. J., Lutowski, C. A., Kantsadi, A. L., Malla, T. R., John, T., Mikhailov, V., Bolla, J. R., Schofield, C. J., Zitzmann, N., Vakonakis, I. & Robinson, C. V. (2020). *Angew. Chem. Int. Ed.* **59**, 23544–23548.
- Emsley, P. & Cowtan, K. (2004). *Acta Cryst. D* **60**, 2126–2132.
- Fan, K., Wei, P., Feng, Q., Chen, S., Huang, C., Ma, L., Lai, B., Pei, J., Liu, Y., Chen, J. & Lai, L. (2004). *J. Biol. Chem.* **279**, 1637–1642.
- Fischer, M. (2021). *Q. Rev. Biophys.* **54**, E1.
- Fodor, J., Riley, B. T., Borg, N. A. & Buckle, A. M. (2018). *J. Immunol.* **200**, 4134–4145.
- Fraser, J. S., van den Bedem, H., Samelson, A. J., Lang, P. T., Holton, J. M., Echols, N. & Alber, T. (2011). *Proc. Natl Acad. Sci. USA*, **108**, 16247–16252.
- Goyal, B. & Goyal, D. (2020). *ACS Comb. Sci.* **22**, 297–305.
- Günther, S., Reinke, P. Y. A., Fernández-García, Y., Lieske, J., Lane, T. J., Ginn, H. M., Koua, F. H. M., Ehrt, C., Ewert, W., Oberthuer, D., Yefanov, O., Meier, S., Lorenzen, K., Krichel, B., Kopicki, J.-D., Gelisio, L., Brehm, W., Dunkel, I., Seychell, B., Gieseler, H., Norton-Baker, B., Escudero-Pérez, B., Domaracky, M., Saouane, S., Tolstikova, A., White, T. A., Hänle, A., Groessler, M., Fleckenstein, H., Trost, F., Galchenkova, M., Gevorkov, Y., Li, C., Awel, S., Peck, A., Barthelmess, M., Schlünzen, F., Lourdu Xavier, P., Werner, N., Andaleeb, H., Ullah, N., Fálke, S., Srinivasan, V., França, B. A., Schwinzer, M., Brognaro, H., Rogers, C., Melo, D., Zaitseva-Doyle, J. J., Knoska, J., Peña-Murillo, G. E., Mashhour, A. R., Hennicke, V., Fischer, P., Hakanpää, J., Meyer, J., Gribbon, P., Ellinger, B., Kuzikov, M., Wolf, M., Beccari, A. R., Bourenkov, G., von Stetten, D., Pompidor, G., Bento, I., Panneerselvam, S., Karpics, I., Schneider, T. R., Garcia-Alai, M. M., Niebling, S., Günther, C., Schmidt, C., Schubert, R., Han, H., Boger, J., Monteiro, D. C. F., Zhang, L., Sun, X., Pletzer-Zelgert, J., Wollenhaupt, J., Feiler, C. G., Weiss, M. S., Schulz, E.-C., Mehrabi, P., Karničar, K., Usenik, A., Loboda, J., Tidow, H., Chari, A., Hilgenfeld, R., Uetrecht, C., Cox, R., Zaliani, A., Beck, T., Rarey, M., Günther, S., Turk, D., Hinrichs, W., Chapman, H. N., Pearson, A. R., Betzel, C. & Meents, A. (2021). *Science*, **372**, 642–646.
- Halle, B. (2004). *Proc. Natl Acad. Sci. USA*, **101**, 4793–4798.
- Jaskolski, M., Dauter, Z., Shabalin, I. G., Gilski, M., Brzezinski, D., Kowiel, M., Rupp, B. & Wlodawer, A. (2021). *IUCrJ*, **8**, 238–256.
- Jin, Z., Du, X., Xu, Y., Deng, Y., Liu, M., Zhao, Y., Zhang, B., Li, X., Zhang, L., Peng, C., Duan, Y., Yu, J., Wang, L., Yang, K., Liu, F., Jiang, R., Yang, X., You, T., Liu, X., Yang, X., Bai, F., Liu, H., Liu, X., Guddat, L. W., Xu, W., Xiao, G., Qin, C., Shi, Z., Jiang, H., Rao, Z. & Yang, H. (2020). *Nature*, **582**, 289–293.
- Kabsch, W. (2010). *Acta Cryst. D* **66**, 125–132.
- Karplus, P. A. & Diederichs, K. (2012). *Science*, **336**, 1030–1033.
- Keedy, D. A., Hill, Z. B., Biel, J. T., Kang, E., Rettenmaier, T. J., Brandão-Neto, J., Pearce, N. M., von Delft, F., Wells, J. A. & Fraser, J. S. (2018). *eLife*, **7**, e36307.
- Keedy, D. A., Kenner, L. R., Warkentin, M., Woldeyes, R. A., Hopkins, J. B., Thompson, M. C., Brewster, A. S., Van Benschoten, A. H., Baxter, E. L., Uervirojnangkoorn, M., McPhillips, S. E., Song, J., Alonso-Mori, R., Holton, J. M., Weis, W. I., Brunger, A. T., Soltis, S. M., Lemke, H., Gonzalez, A., Sauter, N. K., Cohen, A. E., van den Bedem, H., Thorne, R. E. & Fraser, J. S. (2015). *eLife*, **4**, e07574.
- Keedy, D. A., van den Bedem, H., Sivak, D. A., Petsko, G. A., Ringe, D., Wilson, M. A. & Fraser, J. S. (2014). *Structure*, **22**, 899–910.
- Kiefersauer, R., Than, M. E., Dobbek, H., Gremer, L., Melero, M., Strobl, S., Dias, J. M., Soulimane, T. & Huber, R. (2000). *J. Appl. Cryst.* **33**, 1223–1230.
- Kneller, D. W., Phillips, G., Kovalevsky, A. & Coates, L. (2020). *Acta Cryst. F* **76**, 483–487.
- Kneller, D. W., Phillips, G., O'Neill, H. M., Jedrzejczak, R., Stols, L., Langan, P., Joachimiak, A., Coates, L. & Kovalevsky, A. (2020). *Nat. Commun.* **11**, 3202.
- Kneller, D. W., Phillips, G., O'Neill, H. M., Tan, K., Joachimiak, A., Coates, L. & Kovalevsky, A. (2020). *IUCrJ*, **7**, 1028–1035.
- Kneller, D. W., Phillips, G., Weiss, K. L., Pant, S., Zhang, Q., O'Neill, H. M., Coates, L. & Kovalevsky, A. (2020). *J. Biol. Chem.* **295**, 17365–17373.
- Kumar, K. S. D., Gurusaran, M., Satheesh, S. N., Radha, P., Pavithra, S., Thulaa Tharshan, K. P. S., Helliwell, J. R. & Sekar, K. (2015). *J. Appl. Cryst.* **48**, 939–942.
- Lee, J., Worrall, L. J., Vuckovic, M., Rosell, F. I., Gentile, F., Ton, A.-T., Caveney, N. A., Ban, F., Cherkasov, A., Paetzel, M. & Strynadka, N. C. J. (2020). *Nat. Commun.* **11**, 5877.
- Lewandowski, J. R., Halse, M. E., Blackledge, M. & Emsley, L. (2015). *Science*, **348**, 578–581.
- Lu, S., Qiu, Y., Ni, D., He, X., Pu, J. & Zhang, J. (2020). *Drug Discov. Today*, **25**, 177–184.
- Moriarty, N. W., Grosse-Kunstleve, R. W. & Adams, P. D. (2009). *Acta Cryst. D* **65**, 1074–1080.
- Moriarty, N. W., Janowski, P. A., Swails, J. M., Nguyen, H., Richardson, J. S., Case, D. A. & Adams, P. D. (2020). *Acta Cryst. D* **76**, 51–62.
- Noske, G. D., Nakamura, A. M., Gawriljuk, V. O., Fernandes, R. S., Lima, G. M. A., Rosa, H. V. D., Pereira, H. D., Zeri, A. C. M., Nascimento, A. A. F. Z., Freire, M. C. L. C., Oliva, G. & Godoy, A. S. (2021). In *A Crystallographic Snapshot of SARS-CoV-2 Main Protease Maturation Process*. Cold Spring Harbor Laboratory.
- Olson, B., Cruz, A., Chen, L., Ghattas, M., Ji, Y., Huang, K., Ayoub, S. Jr, Luchko, T., McKay, D. J. & Kurtzman, T. (2020). *J. Comput. Aided Mol. Des.* **34**, 1219–1228.
- Panchariya, L., Khan, W. A., Kuila, S., Sonkar, K., Sahoo, S., Ghoshal, A., Kumar, A., Verma, D. K., Hasan, A., Khan, M. A., Jain, N., Mohapatra, A. K., Das, S., Thakur, J. K., Maiti, S., Nanda, R. K., Halder, R., Sunil, S. & Arockiasamy, A. (2021). *Chem. Commun.* **57**, 10083–10086.
- Pearce, N. M. & Gros, P. (2021). *Nat. Commun.* **12**, 5493.
- Ploscuriu, N., Burnley, T., Gros, P. & Pearce, N. M. (2021). *Acta Cryst. D* **77**, 1357–1364.
- Riley, B. T., Wankowicz, S. A., de Oliveira, S. H. P., van Zundert, G. C. P., Hogan, D. W., Fraser, J. S., Keedy, D. A. & van den Bedem, H. (2021). *Protein Sci.* **30**, 270–285.
- Sanchez-Weatherby, J., Bowler, M. W., Huet, J., Gobbo, A., Felisaz, F., Lavault, B., Moya, R., Kadlec, J., Ravelli, R. B. G. & Cipriani, F. (2009). *Acta Cryst. D* **65**, 1237–1246.
- Schneider, D. K., Shi, W., Andi, B., Jakoncic, J., Gao, Y., Bhogadi, D. K., Myers, S. F., Martins, B., Skinner, J. M., Aishima, J., Qian, K.,

- Bernstein, H. J., Lazo, E. O., Langdon, T., Lara, J., Shea-McCarthy, G., Idir, M., Huang, L., Chubar, O., Sweet, R. M., Berman, L. E., McSweeney, S. & Fuchs, M. R. (2021). *J. Synchrotron Rad.* **28**, 650–665.
- Studier, F. W. (2005). *Protein Expr. Purif.* **41**, 207–234.
- Terwilliger, T. C., Grosse-Kunstleve, R. W., Afonine, P. V., Moriarty, N. W., Zwart, P. H., Hung, L.-W., Read, R. J. & Adams, P. D. (2008). *Acta Cryst. D* **64**, 61–69.
- Tickle, I. J., Flensburg, C., Keller, P., Paciorek, W., Sharff, A., Vonnrhein, C. & Bricogne, G. (2018). *STARANISO*, <https://staraniso.globalphasing.org/cgi-bin/staraniso.cgi>. Cambridge, UK: Global Phasing Ltd.
- V'kovski, P., Kratzel, A., Steiner, S., Stalder, H. & Thiel, V. (2021). *Nat. Rev. Microbiol.* **19**, 155–170.
- Vuong, W., Khan, M. B., Fischer, C., Arutyunova, E., Lamer, T., Shields, J., Saffran, H. A., McKay, R. T., van Belkum, M. J., Joyce, M. A., Young, H. S., Tyrrell, D. L., Vederas, J. C. & Lemieux, M. J. (2020). *Nat. Commun.* **11**, 4282.
- Williams, C. J., Headd, J. J., Moriarty, N. W., Prisant, M. G., Videau, L. L., Deis, L. N., Verma, V., Keedy, D. A., Hintze, B. J., Chen, V. B., Jain, S., Lewis, S. M., Arendall, W. B., Snoeyink, J., Adams, P. D., Lovell, S. C., Richardson, J. S. & Richardson, J. S. (2018). *Protein Sci.* **27**, 293–315.
- Winn, M. D., Ballard, C. C., Cowtan, K. D., Dodson, E. J., Emsley, P., Evans, P. R., Keegan, R. M., Krissinel, E. B., Leslie, A. G. W., McCoy, A., McNicholas, S. J., Murshudov, G. N., Pannu, N. S., Potterton, E. A., Powell, H. R., Read, R. J., Vagin, A. & Wilson, K. S. (2011). *Acta Cryst. D* **67**, 235–242.
- Winter, G. & McAuley, K. E. (2011). *Methods*, **55**, 81–93.
- Winter, G., Waterman, D. G., Parkhurst, J. M., Brewster, A. S., Gildea, R. J., Gerstel, M., Fuentes-Montero, L., Vollmar, M., Michels-Clark, T., Young, I. D., Sauter, N. K. & Evans, G. (2018). *Acta Cryst. D* **74**, 85–97.
- Woldeyes, R. A., Sivak, D. A. & Fraser, J. S. (2014). *Curr. Opin. Struct. Biol.* **28**, 56–62.
- Word, J. M., Lovell, S. C., Richardson, J. S. & Richardson, D. C. (1999). *J. Mol. Biol.* **285**, 1735–1747.
- Zhang, L., Lin, D., Sun, X., Curth, U., Drosten, C., Sauerhering, L., Becker, S., Rox, K. & Hilgenfeld, R. (2020). *Science*, **368**, 409–412.